

# ATTRIBUTES FROM NMIS TIME COINCIDENCE, FAST-NEUTRON IMAGING, FISSION MAPPING, AND GAMMA-RAY SPECTROMETRY DATA

Alicia L. Swift<sup>1</sup>, Brandon R. Grogan<sup>2</sup>, James A. Mullens<sup>2</sup>, Jason P. Hayward<sup>1</sup>, and John T. Mihalcz<sup>2</sup>

<sup>1</sup>The University of Tennessee, Knoxville, TN 37996

<sup>2</sup>Oak Ridge National Laboratory, Oak Ridge, TN 37831

## ABSTRACT

This work tests a systematic procedure for analyzing data acquired by the Nuclear Materials Identification System (NMIS) at Oak Ridge National Laboratory with fast-neutron imaging and high-purity germanium (HPGe) gamma spectrometry capabilities. NMIS has been under development by the US Department of Energy Office of Nuclear Verification since the mid-1990s, and prior to that by the National Nuclear Security Administration Y-12 National Security Complex, with NMIS having been used at Y-12 for template matching to confirm inventory and receipts. In this present work, a complete set of NMIS time coincidence, fast-neutron imaging, fission mapping, and HPGe gamma-ray spectrometry data was obtained from Monte Carlo simulations for a configuration of fissile and nonfissile materials. The data were then presented for analysis to someone who had no prior knowledge of the unknown object to accurately determine the description of the object by applying the previously-mentioned procedure to the simulated data. The best approximation indicated that the unknown object was composed of concentric cylinders: a void inside highly enriched uranium (HEU) (84.7±1.9 wt % <sup>235</sup>U), surrounded by depleted uranium, surrounded by polyethylene. The final estimation of the unknown object had the correct materials and geometry, with error in the radius estimates of material regions varying from 1.58% at best and 4.25% at worst; error in the height estimates varied from 2% to 12%. The error in the HEU enrichment estimate was 5.9 wt % (within 2.5σ of the true value). The accuracies of the determinations could be adequate for arms control applications. Future work will apply this iterative reconstructive procedure to other unknown objects to further test and refine it.

## INTRODUCTION

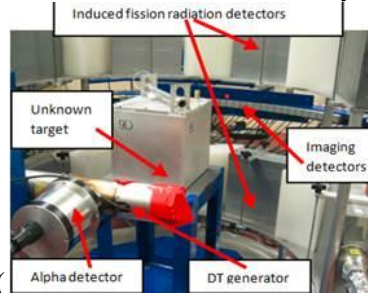
The Nuclear Materials Identification System (NMIS) has been under development at Oak Ridge National Laboratory since 1984 for nuclear material control and accountability applications and then beginning in the mid-1990s for possible future treaty verification applications [1]. It has also been used in other nuclear nonproliferation applications, such as template matching for confirmation of inventories of weapons components [2].

This project used Monte Carlo codes to simulate NMIS time coincidence distributions, fast-neutron imaging, fission mapping, and passive and active time-tagged gamma-ray spectrometry to analyze an unknown configuration of fissile and other materials. The simulated NMIS-type neutron data were obtained with MCNP-PoliMi [3], and the gamma-ray spectrometry data was modeled with MCNPX version 2.6.0 [4]. These simulated data were presented to one of the authors (Alicia Swift), who had no knowledge of the object, for analysis to determine the configuration and materials of the unknown object through a previously determined process [5]. As such, this was a blind study to determine how much information could be obtained from each individual step in the analysis as well as collectively. This process used the provided simulated data to form an initial estimate of the configuration and materials, which was then modeled with MCNP-PoliMi, analyzed, and compared to the provided time distribution of coincidence data to further refine the estimate of the material configuration.

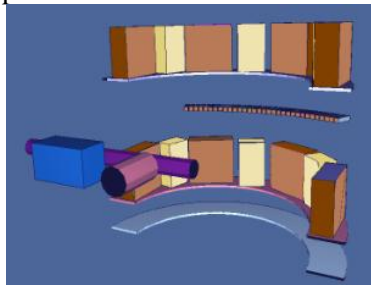
## NMIS MEASUREMENT SYSTEM

NMIS uses a portable deuterium-tritium (D-T) generator (Thermo-Fisher Scientific API120) that employs the reaction  ${}^2_1\text{H} + {}^3_1\text{H} \rightarrow {}^4_2\text{He} + {}^1_0\text{n}$  to generate 14.1 MeV neutrons for active interrogation of unknown objects [5, 6]. Approximately  $4 \times 10^7$  n/s are isotropically produced by aiming a beam of deuterons and

tritons (less than  $60 \mu\text{A}$ ) at a 5 mm diameter zirconium target embedded with tritium and deuterium atoms [2, 7]. The D-T reaction also emits 3.5 MeV alphas traveling in almost opposite directions to those of the neutrons [1]. The generator has an associated alpha detector (cerium-doped yttrium aluminum perovskite scintillator) that defines the direction of the alpha particle and thus tags in time and direction the associated neutron. This is necessary for the coincidence counting used in neutron imaging and fission mapping. Light generated by the scintillator is transferred through a fiber-optic faceplate to a Hamamatsu H9500 pixelated photomultiplier, allowing the neutron beam to be electronically collimated into a 16-

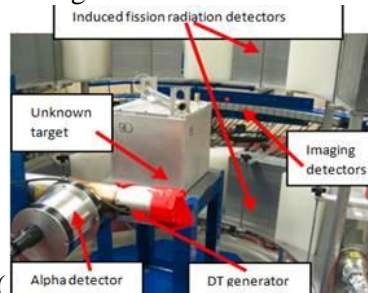


pixel horizontal fan beam for active interrogation (

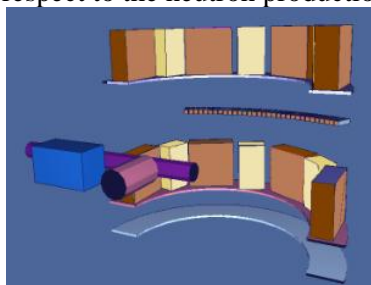


) [5].

NMIS has two types of detectors, the first of which are thirty-two  $2.54 \times 2.54 \times 10.16$  cm plastic EJ-200 transmission imaging detectors. These detectors are arranged along an arc with a 115 cm radius with



respect to the neutron production spot in the D-T generator (



) [7]. This arc was laterally shifted in steps by one-fourth of the distance between the imaging detectors, in a process known as subsampling, to increase the spatial resolution and simulate 128 detector positions [8]. The transmission imaging detector arc can also be raised or lowered to perform a vertical scan along

the height (z-axis) of the object. Additionally, NMIS has eight  $25 \times 25 \times 8$  cm induced fission radiation detectors that are set in a two-tier aluminum array (Figure 1). They are separated by 6 in. of polyethylene to reduce cross talk between detectors and are set in an arc with a 50 cm radius from the center of the interrogation object [9, 10]. These detectors are used for fission mapping and serve the purpose of measuring the multiplicity and obtaining other time coincidence distribution data [8].

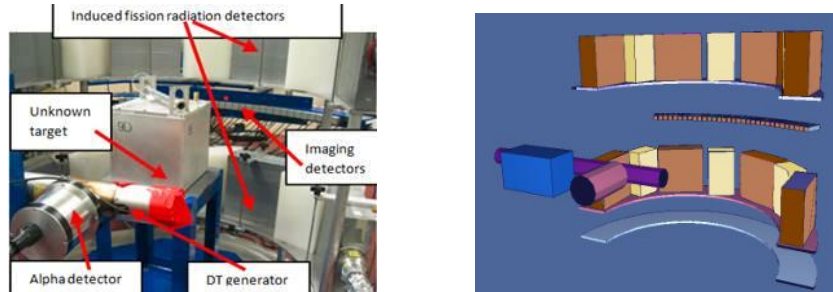


Figure 1. Left: An unknown target is interrogated by a D-T neutron generator with an associated alpha-particle detector; scattered and fission neutrons are then detected with transmission imaging and induced fission radiation detectors on the far side of the object. Right: Diagram of the eight induced fission radiation detectors (dark brown) with polyethylene shielding (light brown). The transmission imaging detectors can be seen in the center (brown), with the D-T generator (blue and purple) and its associated alpha-particle detector (dark pink) shown at the left [8].

An electronics system and data processing are used to compute time correlations in 1 ns increments online between the 16 alpha pixels and each transmission imaging detector and induced fission radiation detector [1]. All correlations are normalized to the source strength through dividing the number of counts in each time interval by the total counts recorded in that pixel over the entire measurement [1, 11]. For more information, see Reference 1.

## DESCRIPTION OF SIMULATED EXPERIMENTAL SETUP

The unknown object was placed on a stainless steel table for both gamma and neutron measurement simulations. The table had dimensions of  $45.72 \times 45.72 \times 1.27$  cm and was at a height of 56 cm above the concrete floor. Passive and active gamma spectroscopy was simulated with MCNPX version 2.6.0. The idealized, simulated high-purity germanium (HPGe) gamma detector was a 3 in. cube placed 1 mm from the surface of the object and  $90^\circ$  to the central pixel of the D-T beam. Detector live time was set to 900 s for both passive and active gamma spectroscopy, and counts were obtained via a normalized F8 tally in the HPGe detector. After total counts were determined, energy spreading was added to the data by assuming an energy resolution of 0.5% at the 661 keV peak. The resolution everywhere else varied from this value by the square root of the energy deposited.

Neutron imaging and fission mapping data were simulated with a source-to-object-center distance of 35 cm, a source-to-imaging-detector distance of 115 cm, and induced fission radiation detectors located 50 cm from object center. A vertical scan was simulated along the height of the object in 1 cm intervals ranging from 54 to 83 cm above the floor. Simulated time correlation data for 60 rotations of  $6^\circ$  each were simulated at a height of 70 cm above the floor, which the vertical scan had indicated was the appropriate height for a radial tomograph. All simulated time correlation data (specifically, transmission, scattered, and neutrons and gammas from fission) was provided from MCNP-PoliMi simulations. The eight induced fission radiation detectors were modeled with a 50 ns dead time and a neutron energy threshold of 1 MeV. Induced fission radiation detector simulations were run separately from transmission imaging detector simulations. The two transmission imaging methods used in this process, filtered back projection (FBP) and maximum likelihood expectation maximization (MLEM) iterative reconstruction,

dictated that a void simulation be performed with no object present ( $I_o$ ), followed by a simulation with the object present ( $I$ ). This is because transmission imaging techniques are based on

$$I = I_o e^{-\mu x}$$

where  $\mu$  ( $\text{cm}^{-1}$ ) is the material-dependent attenuation coefficient for 14.1 MeV neutrons along the path length  $x$  (cm) through the object. Both  $\mu$  and  $x$  are necessary for transmission image reconstruction.

### **INTERPRETATION OF SIMULATED MEASUREMENT DATA**

First, the passive gamma spectrum was analyzed to determine what, if any, fissile or fissionable material was present. The possible presence of highly enriched uranium (HEU) or depleted uranium (DU) (specifically  $^{235}\text{U}$  and  $^{238}\text{U}$  peaks) was identified (Figure 2) [12]. The passive spectrum was then used to estimate the uranium enrichment ( $E$ ) by taking a ratio of the  $^{235}\text{U}$  (e.g., 186 keV) to  $^{238}\text{U}$  (e.g., 258 and 1001 keV) net counts corrected for peak yields [12, 13]. The 186:1001 ratio yielded  $E=0.056$  wt %  $^{235}\text{U}$ , and the 186:258 ratio yielded  $E=0.066$  wt %  $^{235}\text{U}$ , both suggesting the material is DU, which nominally contains 0.2 wt %  $^{235}\text{U}$ . These ratio methods underestimate  $E$  due to different attenuation of the two gamma rays chosen. A second method to estimate  $E$  used GADRAS [13], which employs a multiple regression iterative algorithm that iteratively varies parameters of a simple spherical model, such as materials and enrichment, to generate an estimated spectrum to match the simulated passive spectrum and thus predict enrichment [13]. This GADRAS analysis yielded  $E=0.2$  wt %  $^{235}\text{U}$ , also pointing to the presence of DU. It is thought that there is less uncertainty compared with the first method because GADRAS uses multiple peaks simultaneously (whereas the first method uses only two peaks) and corrects for attenuation. It is important to note at this point that fissile material could be present both interior to and shielded by DU; the presence of HEU will be evaluated at a later stage in the analysis process.

Next, the active gamma spectrum was examined to ascertain the existence of nonfissile material. Significant peak energies from the active spectrum are labeled in Figure 3. The iron seen in the spectrum is most likely a result of (n,n') reactions from the associated alpha pixel in the D-T generator in the stainless steel measurement table that are being detected by the HPGe detector directly above the table. As such, iron may not be present. Note that the carbon peak at 4945 keV and its single and double escape peaks are present in this spectrum. The hydrogen capture gamma ray at 2223 keV and its single and double escape peak are also present. Initially, it was estimated from the gamma-ray spectra that the materials comprising the unknown object were polyethylene and DU.

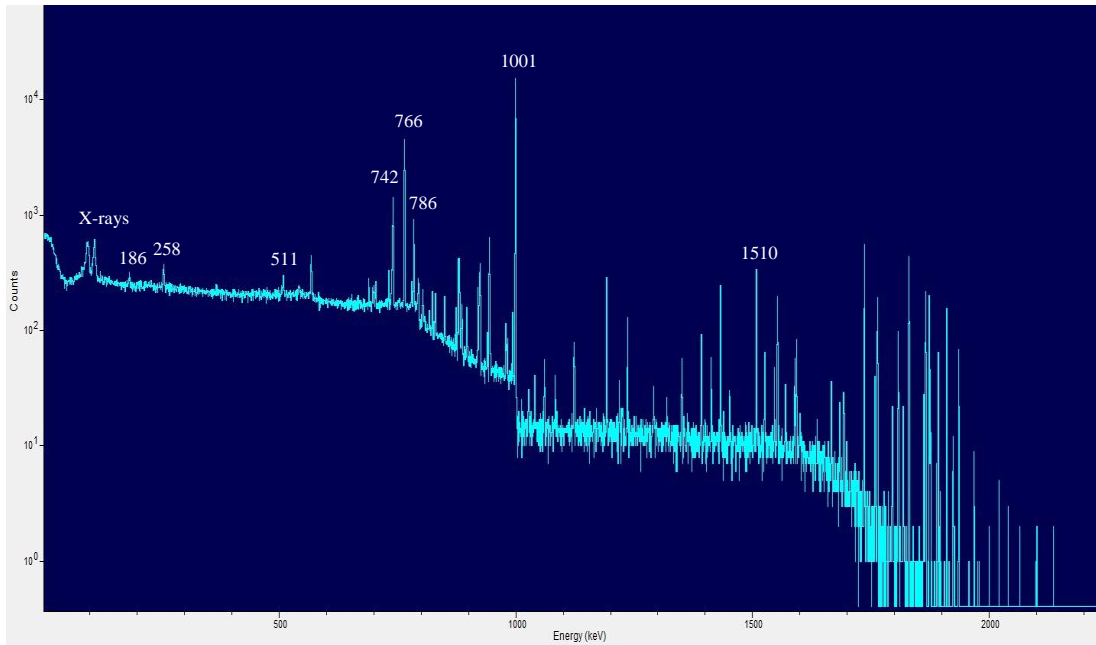


Figure 2. Significant counts in the passive gamma spectra and their energies that indicate the presence of uranium isotopes (in keV): 186, 258, 511, 742, 766, 786, 1001, and 1510.

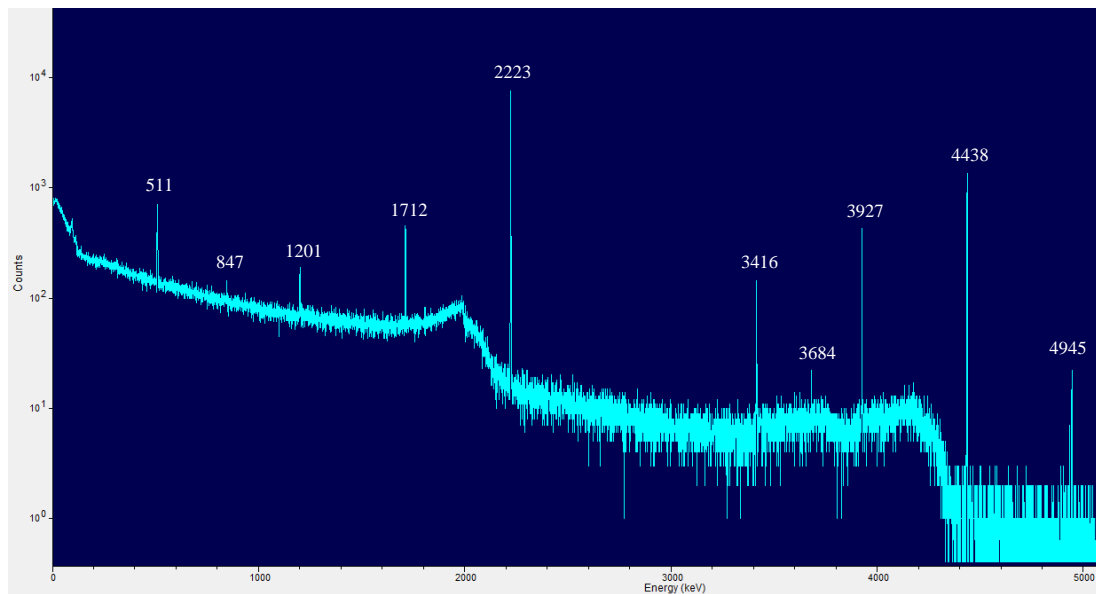


Figure 3. Significant counts in the active gamma spectra and their isotopes and energies (in keV): 511 (pair production peak), 847 (Fe), 1201 (H; double escape peak), 1712 (H; single escape peak), 2223 (H), 3416 (C; double escape peak), 3684 (C), 3927 (C; single escape peak), 4438 (C), and 4945 (C).

The next step was to examine the simulated vertical transmission imaging scan of the object to determine regions of interest and therefore the best height at which to make a detailed radial scan of the object (Figure 4). The vertical center of the object, or 70 cm, was identified as the height at which a radial slice would show all material regions of the object. This vertical scan also allowed for the determination of the height of the material regions in the unknown object using in-house software. This showed that the object was a cylindrical annulus with a top and bottom lid.

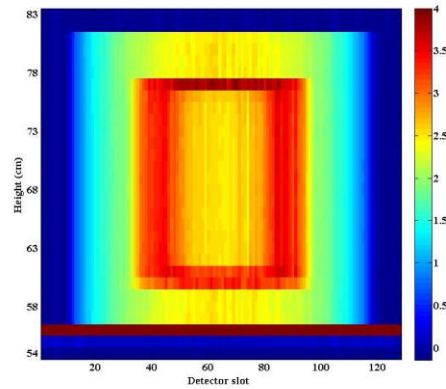


Figure 4. Vertical scan of the unknown object, with red signifying areas of high attenuation length and blue those of low attenuation length.

Next, the transmission neutron imaging data from 60 rotations of the object at a height of 70 cm were analyzed using both FBP and MLEM iterative reconstruction. The FBP algorithm, produced in house, generated a plot of the attenuation coefficient as a function of radial distance. This algorithm summed all of the 60 rotations and took advantage of rotational symmetry to form a radial image of the material regions of the unknown object (Figure 5). Three material regions were delineated according to their attenuation coefficients and the previous gamma spectroscopy: a central void surrounded by DU with polyethylene comprising the outermost region. Region boundaries were approximated by visual inspection of the tomograph; entered into an in-house code, TAKE; and then used, along with regional material attenuation values, to iteratively solve using ray tracing for the locations of the material boundaries, which were used for the final estimate of the unknown object [6]. The second method, MLEM iterative reconstruction, assumed an initial guess of 1 for the attenuation coefficient for each pixel in the tomograph. A ratio of the current-to-previous guess was used as a correction factor to each pixel for a set of specified iterations; in this instance, 50 iterations were performed [6]. The final reconstructed tomographs formed by both methods are shown in Figure 5. Combined with the vertical scan, the radial tomographs showed that the unknown object consisted of a highly attenuating cylindrical shell surrounded by a layer of less attenuating material.

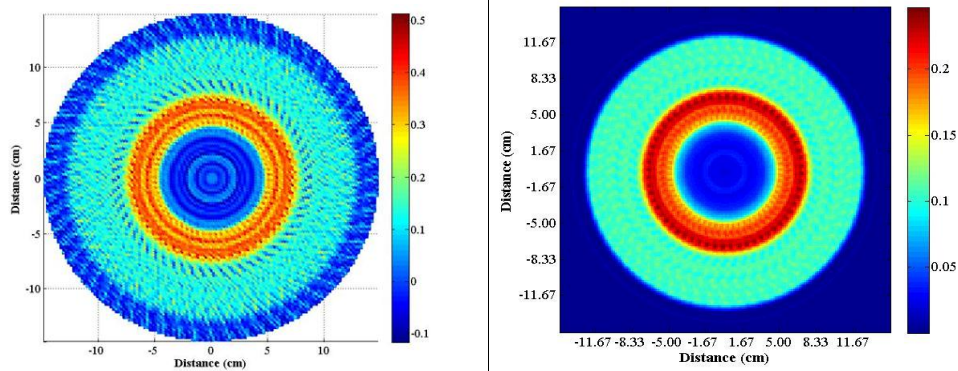


Figure 5. Left: FBP tomograph that plots the attenuation coefficient ( $\text{cm}^{-1}$ ) as a function of radial position (cm). Right: MLEM iterative reconstruction tomograph that plots the attenuation coefficient ( $\text{cm}^{-1}$ ) as a function of transmission imaging pixel number. For both images, areas in red have a high attenuation, while areas in blue have a low attenuation.

Mapping of the fission sites can determine if there is HEU inside the DU, something that cannot be determined from transmission imaging because the attenuation coefficients for HEU and DU metal are

essentially the same. Next, simulated fission mapping data were analyzed by time-correlating single or double coincidences from the induced fission radiation detectors with hits in the associated particle detector's alpha pixels, thereby obtaining two measures of the spatial distribution of fission sites. The higher the number of correlated counts, especially the number of doubles counts, the higher the measure of multiplication along the projection corresponding to the alpha pixel number. The distribution of doubles plotted in Figure 6 shows that alpha pixels 5 through 12 correspond to projections through the target where there is the greatest level of multiplication. This suggests that fissile material such as HEU could be present near the radial center of the target.

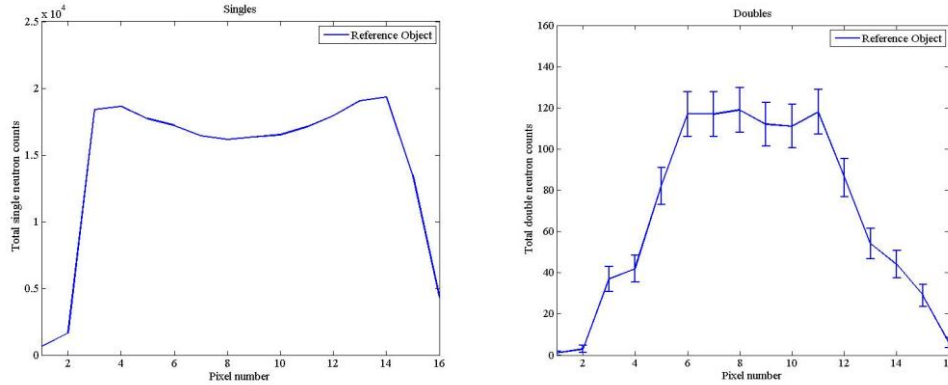


Figure 6. Fission mapping plots for single (left) and double (right) coincidence counts corresponding to hits in the associated particle detector's alpha pixels. Pixels 5 through 12 correspond to projections through the target where there is the greatest level of multiplication.

The next step was to use the MLEM fission reconstruction methodology on the same fission mapping dataset. In this step, an in-house code generated MLEM tomographs of the single and double fission neutron sites (Figure 7) and then overlaid them on a black-and-white version of the MLEM transmission tomograph (Figure 8). The color scale of the MLEM singles and doubles tomographs conveys the number of singles (or doubles) detected per alpha particle. Fifty iterations were conducted in this step. As seen in the doubles overlay in Figure 8, there is a region of medium and high (colored yellow and red, respectively) fission sites surrounded on the outside by a region of low (colored white) fission sites. The doubles reconstruction more accurately determines the region with HEU metal and shows that initial indications (from Figure 7) were correct: the object does indeed have a region of HEU (high multiplication) surrounded on the outside by a dense region of DU (low multiplication). It is important to note that the doubles data provide more insight into the shape of the fissile geometry than the singles data because the D-T neutrons scattered in the target contribute to the singles distribution.

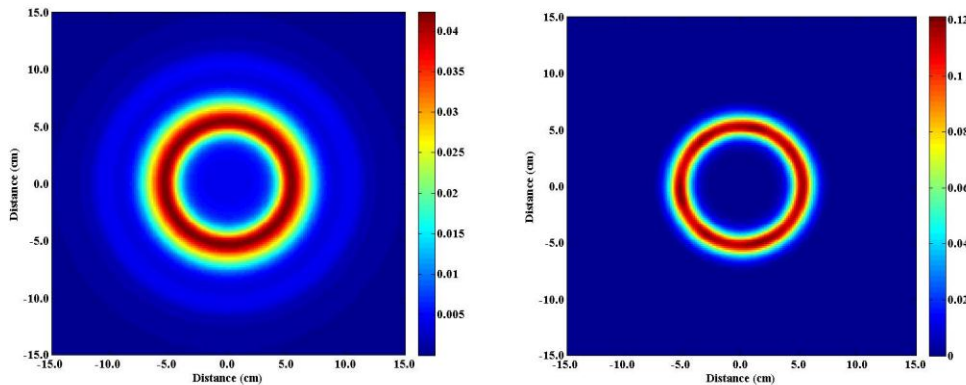


Figure 7. Singles (left) and doubles (right) MLEM reconstruction of the object's tomograph after 50 iterations.

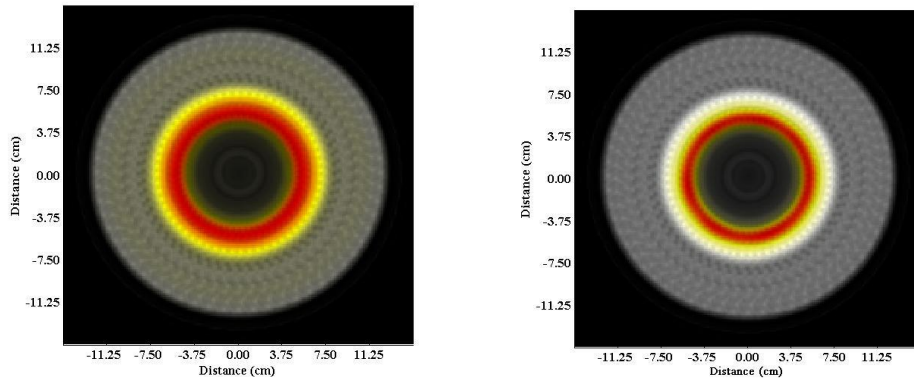


Figure 8. Overlay of the MLEM tomograph reconstruction for singles (left) and doubles (right) coincidence data. Red indicates high values, yellow mid values, and white low values of fission sites.

Once it was determined that HEU and DU were present, a plot of the doubles versus lateral position at the centerline of the doubles tomograph in Figure 7 was used to estimate the boundary between these two material regions (Figure 9). The radius of the boundary was approximated to be halfway between the maximum amount of doubles (corresponding to highest multiplication in HEU) and zero doubles (corresponding to the lowest point of multiplication in DU). Due to the radial symmetry, there were two such locations on the abscissa; converting these into centimeters (division by 6), finding their positive distance from the centerline, and then averaging the two values yielded an outer HEU radius estimate of 6.08 cm.

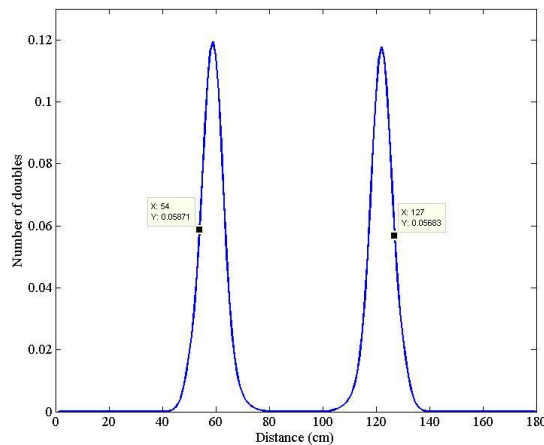


Figure 9. Centerline slice of the MLEM fission reconstruction doubles tomograph. The two peaks correspond to points of maximum multiplication within the cylindrical region of HEU (that was shielded on the outside by a region of DU). This plot was used to determine the radius of HEU in the unknown object.

To estimate the unknown enrichment of the HEU region, a time of flight (TOF)–based interpolation process was conducted. This process required the creation of four MCNP-PoliMi models of the estimated target geometry where the HEU regions varied in enrichment level: 40, 60, 80, and 93 wt %  $^{235}\text{U}$ . The time distributions of coincidences between induced fission radiation detectors and each of the associated particle detector’s alpha pixels, known as TOF distributions, were generated for these four models of varying enrichment and summed over all rotations (Figure 10). It can be seen that photons, traveling at the speed of light, arrive before neutrons at approximately 7 to 10 ns and form a distinct peak. The slight rise in counts after the sharp initial neutron peak is from “late” neutrons—its magnitude being indicative

of fission multiplication and therefore enrichment level. The late neutron window is set from 35 to 80 ns based upon knowledge of the measurement geometry.

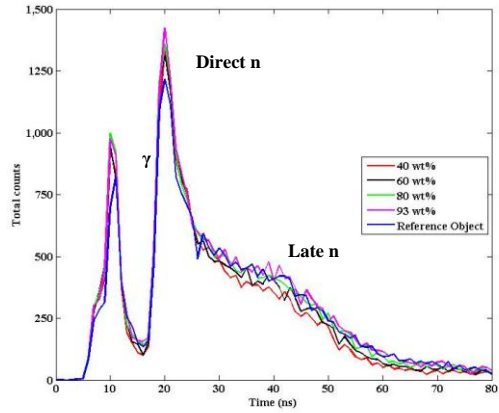


Figure 10. Alpha pixel 9 TOF plot of the total singles counts versus time after associated alpha detection for the four MCNP-PoliMi models (corresponding to four enrichment levels) and the reference data (blue). Gamma ( $\gamma$ ), and direct and late neutron (n) peaks are labeled.

With TOF plots generated for every pixel, the integral of the counts in the region of induced fission radiation detection (i.e., between 35 and 80 ns) was obtained and plotted as a function of enrichment. As established earlier during the fission mapping discussion, only pixels 5 through 12 were associated with the neutrons incident on the HEU region (Figure 6); therefore, only these eight pixels were used for this analysis. The resulting integral versus enrichment data were fit with a weighted second-order polynomial, using the uncertainty, calculated as the square root of the integrated counts, as the weight (Figure 11). The tabulated counts from the reference object were then integrated over the same window of 35 to 80 ns for each of the eight alpha pixels and used to interpolate from the eight enrichment curves (see Figure 11 for an example). These values were then averaged to yield an estimated HEU enrichment value of 84.7 wt %  $^{235}\text{U}$ , with  $1\sigma$  (68.3%) probability of being between 82.8 and 86.6 wt %  $^{235}\text{U}$ . Trends across the alpha pixels can be seen in Figure 12.

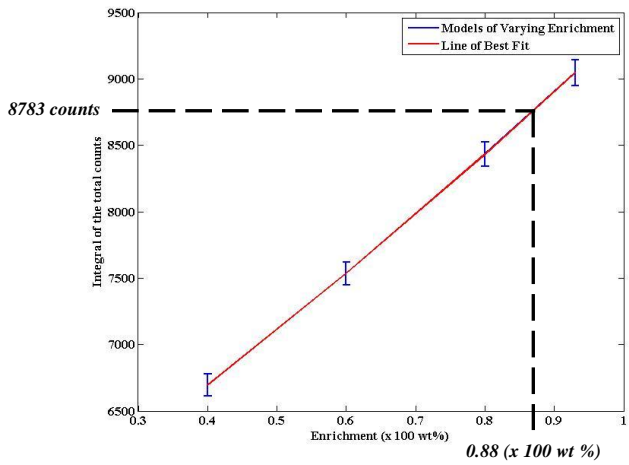


Figure 11. Alpha pixel 9 enrichment curve generated from the integral of the four MCNP-PoliMi models' TOF plots from 35 to 80 ns. Error was taken to be the square root of the integrated counts. The interpolation method used to determine the enrichment of the HEU region of the unknown object is also illustrated; 8783 counts from the reference data for pixel 9 yielded an estimated enrichment of 88.0 wt %  $^{235}\text{U}$ .

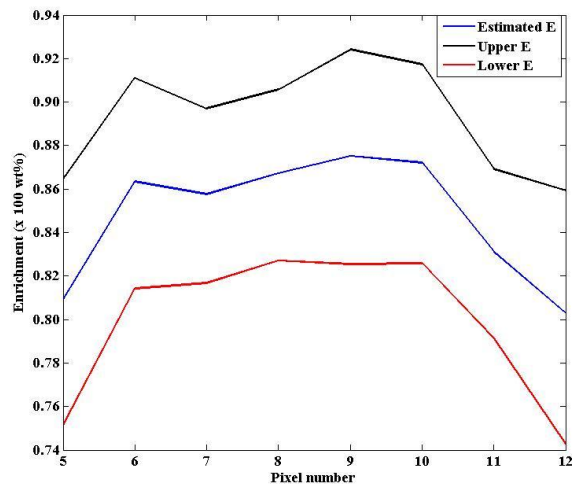


Figure 12. Estimated enrichment (blue) as a function of alpha pixel number. Error is  $2.5\sigma$  (red and black).

### DESCRIPTION OF THE UNKNOWN OBJECT

After the completion of the process outlined above, the final estimate of the object was a multilayered cylindrical object with the estimated dimensions and material regions listed in **Error! Not a valid bookmark self-reference.**. Actual dimensions are also listed in **Error! Not a valid bookmark self-reference.**. The final HEU enrichment estimate was  $84.7 \pm 1.9$  wt %  $^{235}\text{U}$ , which is within  $2.5\sigma$  of the actual value of 80.0 wt %  $^{235}\text{U}$ . The actual geometry is also listed in **Error! Not a valid bookmark self-reference.** for comparison. The radial dimensions obtained were within 1 to 4 mm of the actual values. Most of the error resulted from the heights of the components of the unknown object, which were derived from the vertical transmission scan. This systematic error resulted from the vertical scan image being less clear than the radial scan. Enrichment estimates (and therefore  $^{235}\text{U}$  mass) would have also been more accurate with more accurate radial and height dimensions; enrichment would have decreased to compensate from 84.7 wt % toward the actual enrichment of 80.0 wt %  $^{235}\text{U}$  due to multiplication [14].

Table 1. Final estimate and actual geometry of the unknown object

Material Region	Estimated Radius (cm)	Actual Radius (cm)	Radial Error (%)	Estimated Height (cm)	Actual Height (cm)	Height Error (%)
Void	4.609	4.445	3.69	17	15.24	12
HEU	6.080	6.350	-4.25	17	15.24	12
DU	7.500	7.620	-1.58	19	17.80	7
Polyethylene	12.352	12.700	-2.74	25	25.40	-2

### SUMMARY AND CONCLUSIONS

In a comparison of the final estimated dimensions to the actual dimensions, the error between the estimated and actual geometry varied. Radially, relative error in dimensions varied from 1.58% to -4.25%, with the greatest error in the HEU region; heightwise, relative error in dimensions ranged from -2% to 12%. Relative error in the amount of kilograms of  $^{235}\text{U}$  present in the HEU was -9.7%, which corresponded to an error in the estimate of the enrichment of 5.9 wt %. The bulk of the error was introduced through systematic error from the algorithm that conducted the vertical neutron transmission image reconstruction. These accuracies may be adequate for possible use in future treaty verifications.

Further study of additional objects should shed more light on accuracy for various unknown object compositions and configurations.

In summary, it is possible to quantitatively determine the materials present and their configuration by iterative analysis using passive and active gamma spectroscopy, FBP and MLEM neutron transmission tomographs (including radial and vertical scans), neutron coincidence and multiplicity counting, and fission mapping data. The unknown object presented here represents a case that was particularly challenging because the fissile material was surrounded by DU. Even so, the region that contained the HEU was identified, and its enrichment was estimated within 5 wt %, or  $2.5\sigma$ , of the actual value, considering the uncertainty inherent in the estimation technique. In future work, it may be possible to reduce uncertainties and determine how well this technology will apply to future treaty verification applications.

### ACKNOWLEDGEMENTS

This manuscript has been authored by UT-Battelle, LLC, under Contract No. DE-AC05-00OR22725 with the US Department of Energy. The United States Government retains and the publisher, by accepting the article for publication, acknowledges that the United States Government retains a nonexclusive, paid-up, irrevocable, worldwide license to publish or reproduce the published form of this manuscript, or allow others to do so, for United States Government purposes.

### REFERENCES

1. J. T. Mihalcz, J. A. Mullens, J. K. Mattingly, and T. E. Valentine, "Physical description of nuclear materials identification system (NMIS) signatures," *Nuclear Instruments and Methods in Physics Research A* 450, 531–555 (2000).
2. J. T. Mihalcz, J. K. Mattingly, J. S. Neal, and J. A. Mullens, "NMIS plus gamma spectroscopy for attributes of HEU, PU, and HE detection," *Nuclear Instruments and Methods in Physics Research B* 213, 378–384 (2004).
3. MCNP-PoliMi, <http://www-rsicc.ornl.gov/codes/ccc/ccc7/ccc-718.html>.
4. MCNPX, <http://mcnpx.lanl.gov>.
5. J. Mihalcz and J. Mullens, *Nuclear Material Identification System with Imaging and Gamma-Ray Spectrometry for Plutonium, Highly Enriched Uranium, High Explosives, and Other Materials*, ORNL/TM-2012/22, Oak Ridge National Laboratory, Oak Ridge, Tenn. (February 2012).
6. G. F. Knoll, *Radiation Detection and Measurement*, third ed., 26–27 (2000).
7. B. R. Grogan, J. T. Mihalcz, S. M. McConchie, and J. A. Mullens, "Identification of shielding material configurations using NMIS imaging," *52nd Annual INMM Meeting Conference Proceedings* (July 17, 2011).
8. J. Mullens, S. McConchie, P. Hausladen, J. Mihalcz, B. Grogan, and E. Sword, "Neutron radiography and fission mapping measurements of nuclear materials with varying composition and shielding," *52nd Annual INMM Meeting Conference Proceedings* (July 2011).
9. K. Peña, S. McConchie, J. Crye, and J. Mihalcz, "Active interrogation observables for enrichment determination of DU shielded HEU metal assemblies with limited geometrical information," *52nd Annual INMM Meeting Conference Proceedings* (July 2011).
10. B. R. Grogan and J. T. Mihalcz, "Simulating NMIS imaging and fission-mapping measurements," *52nd Annual INMM Meeting Conference Proceedings* (July 2011).
11. B. R. Grogan, S. M. McConchie, J. T. Mihalcz, and J. A. Mullens, "Alpha detector pixelation effects on NMIS imaging," *49th Annual Meeting of the Institute of Nuclear Materials Management Conference Proceedings* (November 2008).
12. G. W. Phillips, D. J. Nagel, and T. Coffey, *A Primer on the Detection of Nuclear and Radiological Weapons*, Center for Technology and National Security Policy, National Defense University (2005).

13. GADRAS, <http://www-rsicc.ornl.gov/codes/psr/psr5/psr-560.html>.
14. J. Duderstadt and L. Hamilton, *Nuclear Reactor Analysis*, Wiley, 84 (1976).